Final focus system for high intensity beams

Enrique Henestroza, Shmuel Eylon, Prabir K. Roy, Simon S. Yu, Frank M. Bieniosek,
Derek B. Shuman, and William L. Waldron

Lawrence Berkeley National Laboratory, University of California, Berkeley, California 94720, USA

(Received 30 June 2004; published 20 May 2005)

The neutralized transport experiment (NTX) at the Heavy Ion Fusion Virtual National Laboratory is exploring the performance of neutralized final-focus systems for high perveance heavy ion beams. The final-focus scenario in a heavy ion fusion driver consists of several large aperture quadrupole magnets followed by a drift section in which the beam space charge is neutralized by a plasma. This beam is required to hit a millimeter-sized target spot at the end of the drift section. The objective of the NTX experiments and associated theory and simulations is to study the various physical mechanisms that determine the final spot size (radius r_s) at a given distance (f) from the end of the last quadrupole. In a fusion driver, f is the standoff distance required to keep the chamber wall and superconducting magnets properly protected. The NTX final quadrupole focusing system produces a converging beam at the entrance to the neutralized drift section where it focuses to a small spot. The final spot is determined by the conditions of the beam entering the quadrupole section, the beam dynamics in the magnetic lattice, and the plasma neutralization dynamics in the drift section. The main issues are the control of emittance growth due to high order fields from magnetic multipoles and image fields. In this paper, we will describe the theoretical and experimental aspects of the beam dynamics in the quadrupole lattice, and how these physical effects influence the final beam size. In particular, we present theoretical and experimental results on the dependence of final spot size on geometric aberrations and perveance.

DOI: 10.1103/PhysRevSTAB.8.052801 PACS numbers: 52.58.Hm

I. INTRODUCTION

The topic of final-focus systems for high intensity beams has been an important subject of analytical [1–4], and experimental [5] efforts since the beginning of the Heavy Ion Fusion project in 1976. The first designs were derived from systems already in use in particle accelerators for high energy physics where space charge is negligible, and which incorporated sextupoles and octupoles elements for the correction of chromatic and geometric aberrations. Chromatic aberrations affect the focal spot radius due to deviations from the nominal ion momentum causing a variation in the focal length produced by the magnet system. These aberrations may result from initial transients in the injector, from residual momentum tilt due to beam compression, or from the momentum spread, or longitudinal emittance produced along the beam line. Geometric aberrations are due to nonlinear external fields and also from deviations from paraxial ray optics.

In a possible scenario of a final-focus system for a heavy ion fusion (HIF) driver, the beam is transported in the final-focus section through several strong large aperture magnetic quadrupoles, and is then allowed to drift ballistically through neutralizing plasma in a low-density (millitorr) gas onto the target. There are nonlinear processes both in the magnetic section as well as in the neutralized transport section. To investigate these phenomena, the neutralized transport experiment (NTX) has begun at LBNL [6]. The NTX beam line (Fig. 1) consists of 4 large bore quadrupoles followed by a neutralized drift section. A low emittance K^+ beam is made to traverse this 4-quad lattice, at the exit of which, the beam enters a 1-meter-long drift section with injected plasma. The beam is diagnosed at the exit of the 4-quad section as well as the end of the drift section.

The relevance of NTX to the fusion driver is derived from the observation that the key scaling parameter is perveance, defined as

$$Q = \frac{1}{4\pi\varepsilon_0}\frac{2ZeI_b}{m_i v_i^3}, \tag{1}$$

where I_b is the beam current, and Z , m_i, and v_i are, respectively, the charge state, mass, and velocity of the beam ions. The beam dynamics of a low current, low energy beam, as in NTX, is identical to a high current, high energy beam in a fusion driver, as long as the perveance is the same, and the focusing fields are scaled appropriately (Sec. II).

In the NTX experiment the injector is designed to generate a very high-brightness, space-charge-dominated potassium beam where the perveance is varied by means of a beam aperturing system immediately downstream of the ion source and upstream of the first quadrupole. By changing the aperture size, we vary the beam current at a fixed energy.

A simple theoretical model for neutralized drift provides us the framework in which to analyze the more detailed experiments and simulations. For a beam, which is nearly ballistic, the focal length f is given by

$$f = \frac{r_0}{\theta}, \tag{2}$$

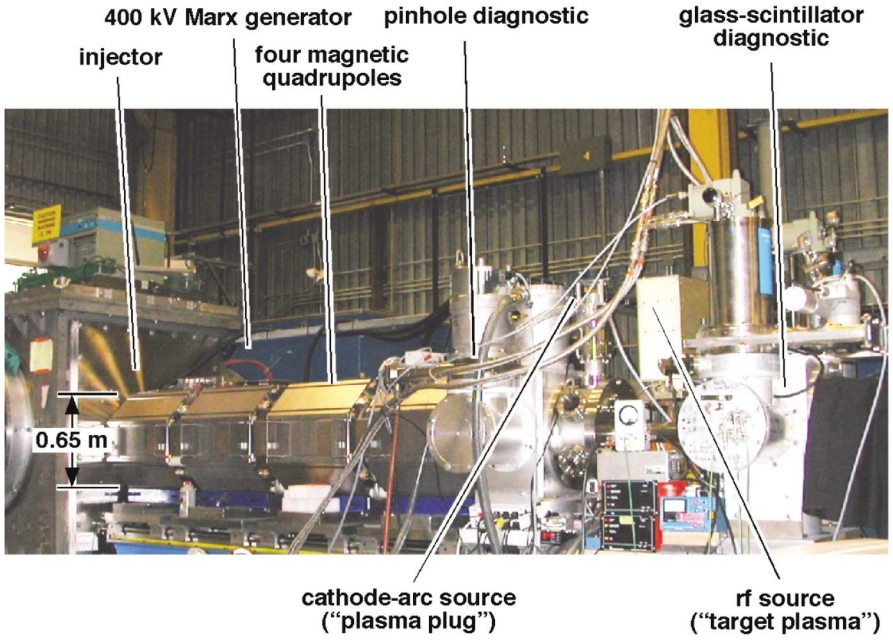

FIG. 1. (Color) neutralized transport experiment (NTX).

where r_0 is the beam radius and θ is the angle of convergence at the entrance of the drift section (i.e., exit of the quadrupole lattice). The final spot size r_s at the focal point is given by

$$r_s = \frac{\varepsilon}{\theta}, \tag{3}$$

where ε is the unnormalized emittance of the beam at target.

The first question, addressed with a combination of simulations and experiment, is whether we can place the focal spot at target, more specifically, whether we can control the beam in the quadrupole lattice to produce any desired beam size r_0 and convergence angle θ at the entrance to the drift section. Beam control is obtained by changing the magnetic strength of the 4 quadrupoles. We have varied the quadrupoles to obtain various values of θ (5, 10, 15, and 20 mr) for a given beam energy and current. The agreement between theory and experiment is excellent. We have also varied individual quadrupole strengths, and demonstrated that the beam shape changes in a predictable manner. In addition, the beam energy (and current) was varied, and again, the beam shape varied in a predictable manner. Finally, the perveance was varied, and the same code/experiment agreement was demonstrated.

The ultimate objective for the fusion application is to deliver the entire pulse onto the target with the same small spot. This is a nontrivial task because the beam energy and current from head to tail is not uniform. The different slices of the beam may have somewhat different beam envelopes through the magnetic lattice, leading to different beam size and convergence angle, and therefore variable focal length from head to tail. We need to know the sensitivity of the beam optics to small changes in beam energy. To evaluate this effect, we measured the beam size as the energy varied. We observed that energy variations of 1% led to reduction of current density by 50%. This experimental result is consistent with theory. We also measured directly the spot size variation from head to tail and significant changes were observed. The voltage waveform shows a variation of $\sim$1%, and this energy variation is enough to account for the head-to-tail variation in spot size. For future work, we need to study the energy sensitivity for other lattices (e.g., 6-quad lattice) to see if the energy sensitivity could be reduced. Also, time-dependent focusing may be used to correct for the head-to-tail variations.

This paper describes the experiments and associated theory and simulations to study the various physical mechanisms in the magnetic lattice that affect the final spot size (radius r_s) at a given distance (f) from the end of the last quadrupole of the neutralized transport experiment. The physics of final-focus magnetic lattice, in the context of neutralized drift, is reviewed in Sec. II, including the effects of geometric and chromatic aberration on the final spot size. In Sec. 3, we describe the NTX beam-line layout and diagnostic suite as well as the numerical particle-in-cell simulation code WARP3D [7]. The improved measurement techniques are essential for quantitative validation of code predictions. Section IV presents the measurements of beam transport through the magnetic lattice and comparison with simulations made using the WARP3D code, and includes the control of convergence angle, energy sensitivity and shift of focus, geometric aberrations and emittance growth, and perveance scaling. Section V describes several factors that influence the interpretation of the experimental results, including secondary electron effects,

energy calibration, measurement of quadrupole field strength, and efficiency of the diagnostic devices. Conclusions are presented in Sec. VI.

II. FINAL-FOCUS MAGNETIC LATTICE

The NTX transport section is designed to correspond closely to a prototypical HIF driver final-focus channel. It consists of four pulsed quadrupole magnets with short drift regions, including the drift from the source into the channel and the drift from the channel to the plasma neutralization chamber. For a beam with a uniform transverse current density, the description of the beam transverse size along the channel is given to first order by the envelope equations of Kapchinskij and Vladimirskij [8]

$$\frac{d^2a}{dz^2} = Ka + \frac{2Q}{a+b} + \frac{\varepsilon_x^2}{a^3}, \tag{4}$$

$$\frac{d^2b}{dz^2} = -Kb + \frac{2Q}{a+b} + \frac{\varepsilon_y^2}{b^3}, \tag{5}$$

where a and b are the transverse edge dimensions, z is the dimension along the quadrupole lattice centerline, K is the quadrupole force given by $B'/[B\rho]$, B' is the magnetic field gradient, and $[B\rho]$ is the beam rigidity. The space-charge force is proportional to the perveance Q and the phase-space pressure is given by the unnormalized emittance ε_x and ε_y. For a given perveance and unnormalized emittance, the beam envelopes do not change when the magnetic field is transformed proportional to the rigidity; and for a given perveance and rigidity, the beam envelopes are self-similar when the emittance is proportional, and the magnetic field is inversely proportional to the beam size. For NTX, $Q \sim 0.0006$, corresponding to a 25 mA potassium beam at 300 keV. An equal perveance driver beam will correspond to a 10 kA Xenon beam at 2.5 GeV. It is worth noticing that during the final-focus transport the beam dynamics is space-charge dominated, and becomes emittance dominated when the beam approaches the focal plane.

Figure 2 shows the horizontal and vertical beam envelopes through the NTX system, with and without beam neutralization after the final-focus lattice. The quadrupole fields are chosen to obtain a beam of one-meter focal length (20 mm radius, and 20 mr convergence) at the entrance to the neutralization region.

The heavy ion beam is space-charge dominated in the final-focus system, where it has a large cross section and is highly nonparaxial. The beam expands in the two center magnets, which determines the amount of nonlinear magnetic fields that the beam samples as well as the degree of nonparaxial motion. These geometrical aberrations will change the focusing properties calculated by the envelope equations. Therefore, particle tracking simulations require the knowledge of the multipole field content of the magnetic field. It can be shown [1] that to third order the main

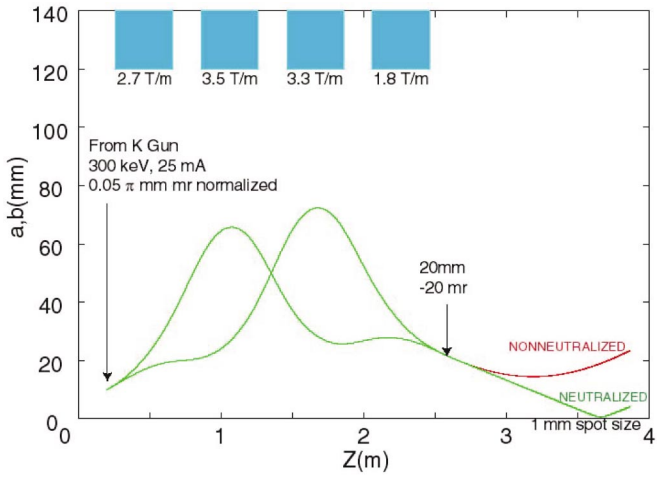

FIG. 2. (Color) Final-focus lattice for ballistically neutralized drift.

contribution to the beam dynamics come from the normal quadrupole, the normal sextupole and the pseudooctupole components of the magnetic field. These three components are included in all the numerical simulations performed for the design of the lattice.

Neuffer [1] has shown that the geometric aberrations depend only on the nonperturbed (first order) particle trajectories; therefore the scaling properties of the geometric aberrations for a final-focus system depend only on the perveance Q, if the scaled field reproduces the multipole components of the original field. He also found a formula to estimate the correction (increase) of the spot size [Eq. (3)] due to geometric aberrations:

$$\Delta r_s \approx 1350 l_{\text{quad}} \theta^3, \tag{6}$$

where l_{quad} is the length of the last quadrupole magnet and θ is the convergence angle in radians. For NTX the unnormalized emittance $\varepsilon \sim 20\ \pi$-mm-mr, the convergence angle $\theta \sim 20$ mr, and $l_{\text{quad}} \sim 0.4$ m, from which we get $r_s \sim 1$ mm, and $\Delta r_s \sim 4$ mm. In Sec. 3 we will show that experimentally and numerically we get $\Delta r_s \sim 0.5$ mm, about a factor of 10 less increase in spot size due to geometric aberrations. The discrepancy comes from the fact that the estimate [Eq. (6)] was obtained by analyzing a specific lattice configuration (a quadrupole doublet) which is very different from the NTX lattice.

For fusion applications we require that the final-focus system will deliver the entire beam pulse onto the target with the same small spot size. Chromatic aberrations affect the focal spot radius due to deviations from the nominal ion momentum causing a variation in the focal length produced by the magnet system, and can be separated into two types. The first kind of chromatic aberrations depends on the velocity and current change from beam head to tail and it results from initial transients in the injector, from voltage errors in the accelerating gaps, and from residual momen-

tum tilt due to beam compression. In this case the different slices of the beam may have somewhat different beam envelopes through the magnetic lattice, leading to different beam size and convergence angle, and therefore variable focal length from head to tail. The second kind of chromatic effects depends on the momentum spread at a given beam slice (longitudinal emittance) and is produced along the beam line by thermalization of velocity errors. For a driver there is a requirement to keep the relative momentum spread $\delta p/p \sim 0.1\%$, and remove the velocity tilt by the time the beam reaches the focal plane.

An estimate of the correction (increase) of the spot size [Eq. (3)] due to chromatic aberrations from momentum spread was obtained by Lee [9]:

$$\delta r_s \approx 6 f \theta \left(\frac{\delta p}{p}\right), \tag{7}$$

where f is the focal length of the last quadrupole magnet, θ is the convergence angle in radians, and $\delta p/p$ is the beam momentum spread. For NTX the focal length $f = 1$ m, the convergence angle $\theta \sim 20$ mr, and $\delta p/p \sim 0.1\%$, from which we get $\Delta r_s \sim 0.1$ mm. Hence, spot size increase due to chromatic aberrations from momentum spread is negligible on NTX. Equation (7) includes the partial cancellation of chromatic effects by the space charge of a uniform density beam. The effects of beam space charge on the beam dynamics also include nonlinear forces arising from nonuniform charge density distribution as well as image forces from the beam pipe. These effects depend on the length of the lattice and the clearance between the edge of the beam and the walls of the chamber, and are negligible for a short system as NTX.

It is possible to infer the effects of momentum spread by studying the sensitivity of the beam parameters to small changes in energy for a given beam slice. This can be evaluated by measuring the beam size as the energy is varied for a given beam slice.

III. EXPERIMENTAL AND NUMERICAL METHODS

Figure 3 shows a sketch of the NTX beam line, consisting of an ion beam injector, 4 quadrupoles and a meter-long neutralized drift section with a cathode arc plasma plug, an rf plasma source, and diagnostics. Optical scintillators imaged by CCD cameras and mechanical slit scanners [6] were used to measure the beam profiles and phase-space distributions of the beam at the end of the final-focus lattice.

The K^+ beam is produced within the source chamber by a standard hot plate [10] of a 2.54 cm diameter aluminosilicate source across a diode with a 12 cm gap. The pulsed power is provided by a Marx generator and crowbar switch that were used in the multiple beam test experiment (MBE-4) [11]. This Marx generator produces a pulse with 0.5–1 μs rise time and is crowbared to produce a 6-μs "flat top." A smooth uniform bright beam profile is generated by increasing the source temperature, smoothing the source surface and aperturing the beam [6]. The use of an aperture to vary the perveance also generates a high-brightness beam by removing the edge of the beam after it exits the diode. Beam scraping, however, produces secondary electrons that are controlled by an electron trap. Figure 4(a) shows a sketch of the beam scraper system, as designed using the EGUN code, and 4(b) a photograph of the aperture and electron trap located at the exit of the NTX diode. The trap consists of two metal tubes, each of 5 cm length, and 6.2 cm inner diameter with an aperture plate in between. The upstream and downstream tubes are located 0.8 cm from the aperture plate. A nominal negative 3 kV

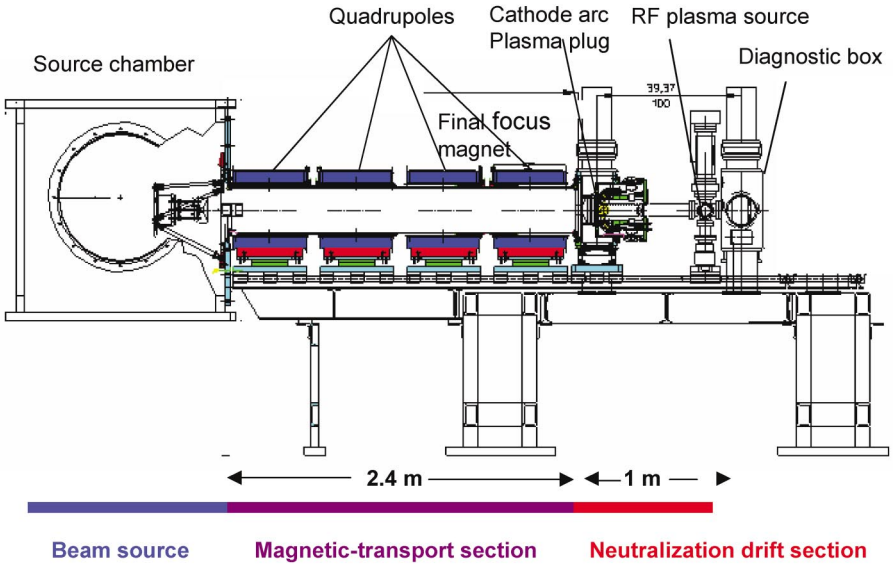

FIG. 3. (Color) Schematic of the NTX beam line.

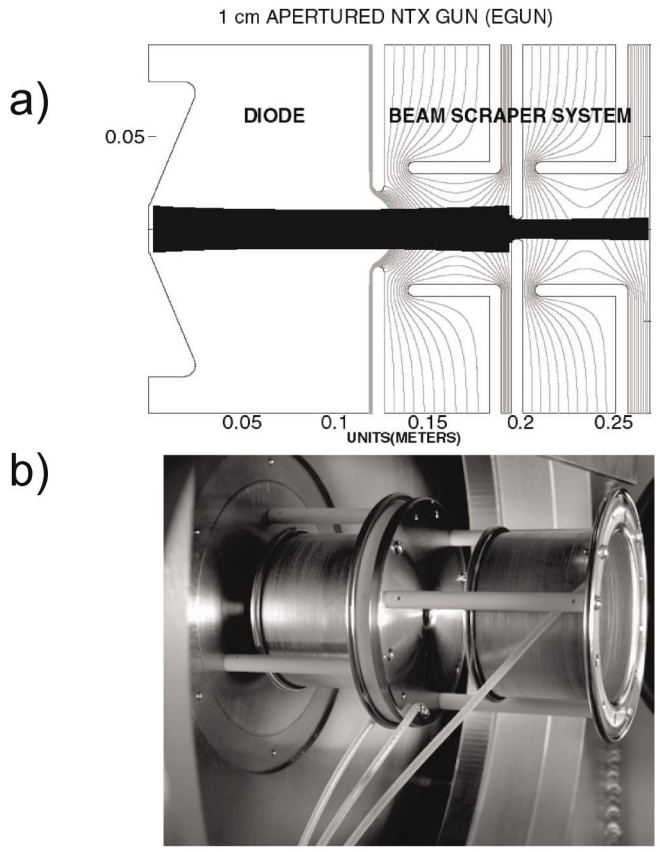

FIG. 4. (a) Equipotential plot of the beam scraper system, and (b) aperture and electron trap system located at the exit of the NTX diode.

potential is provided on each of the metal tubes, providing adequate electron trapping in the presence of the ion beam. Another electron trap, 7.5 cm in radius, is located at the downstream end of the beam line, 10.16 cm downstream from the last quadrupole magnet. A nominal negative 7 KV voltage is used across this second trap to make it effective for collection of stray electrons.

The transport section consists of a double FODO channel with very short drift regions, including the drift from the source into the channel, and the drift into the plasma neutralization chamber. Figure 2 shows the calculated beam envelope (X and Y) through the system. The beam is quite large in the two center magnets, which determines the required bore size and winding radius. The magnet has a relatively short center section and a substantial portion of the magnetic field is contained in the end fringe fields, with significant axial components. The beam is transported through a 2.4 m long path magnetic section, as shown in Fig. 3, using four pulsed quadrupole magnets, as mentioned earlier. The distance from the beam aperture radius to the center of the first magnet, the quadrupole length, and the quadrupole to quadrupole spacing are 26, 46.50, and 60 cm, respectively. Field gradient and maximum field of a magnet are calculated to be 2–5 T/m and 0.6 T, respectively, with a current range of 3.3 to 8.2 kA. The pulser for each NTX quadrupole magnet consists of a bipolar-charged 2 mF capacitor which is discharged through thyristors to produce a current half-sine wave with a pulse width of 2.3 ms. Bipolar charging and a large capacitance were chosen to minimize the voltage from the magnet leads to the grounded magnet housing for the maximum design current. The pulser output voltage is monitored with a resistive voltage divider and the magnet current is monitored with a current transformer. Inside the magnetic lattice, a thin wall (3.3 mm) stainless steel tube of 13 cm inner radius is installed. Eddy currents were calculated by transient 2D finite element analysis, and it was found to result in a 7.4% loss of peak field, and a 275 ms peak field time lag from the source current peak. It was observed that the measured axial field falloff profile agreed well with the computational model [12]. Our measurements with and without stainless steel tube also agree well with the calculations.

The final section of the beam line is known as the neutralized drift section, consisting of a cathode arc plasma plug and an rf plasma source. This section is 1-m long, and beam diagnostics are installed at the end of the drift section to measure nonneutralized and neutralized beams.

Several diagnostics have been used to characterize the ion beam. The primary diagnostics for this experiment consist of (1) a Faraday cup, (2) a slit /slit-cup system, and (3) a scintillator with a gated CCD camera system. The Faraday cup and the slit cup each consists of a collector and a guard ring (grid) with bias voltages that are controlled to collect beam ions only. In addition, we can also monitor currents flowing through the aperture plate and each of the two electron traps. The removable Faraday cup is inserted into the NTX beam line at the exit of the injector and at the end of the magnetic lattice to measure total beam current. The slit/ slit-cup arrangement is used to measure the line-integrated beam profile (with slit cup only) and emittance (with slit and slit cup) at the same locations. The beam profile is measured optically using a glass or ceramic (96% alumina) scintillator with associated camera. Charge neutralization of this scintillator is provided by a high-transparency (80%–90% transmission) metallic mesh placed on or near the surface of the scintillator. By applying a negative bias to the mesh, stray external electrons are decelerated and deflected away from the scintillator, limiting their contribution to the optical image to negligible levels. Time-resolved beam-induced images on the scintillator screen are captured with a Roper Scientific gated intensified CCD camera viewing the scintillator through a vacuum window, and images were processed using the public domain program IMAGEJ.

We are developing a new technique to measure the 4-dimensional phase-space distribution of the beam using the beam imaging diagnostics [6]. The phase-space distribution $f(x, y, x', y')$ can be measured by scanning the beam

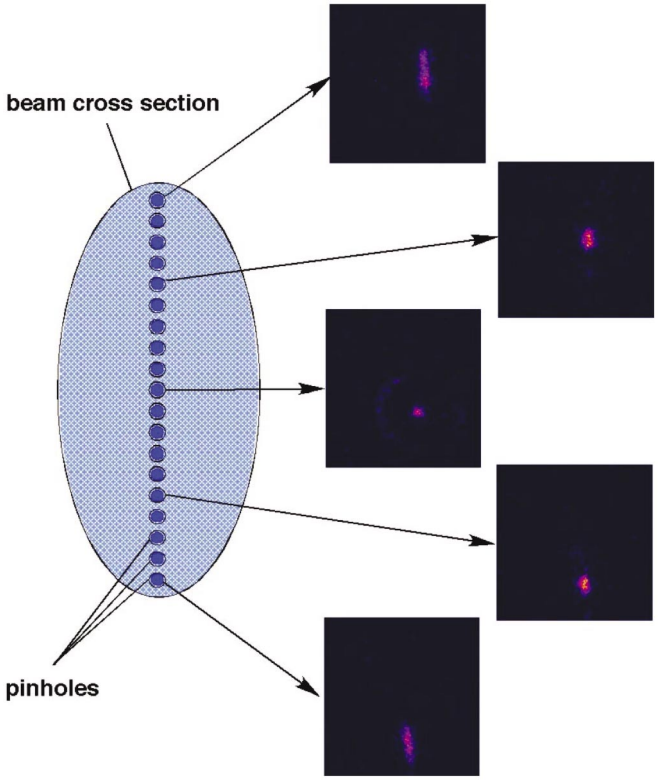

FIG. 5. (Color) Beam imaging technique to measure the phase-space distribution $f(x, y, x', y')$.

with a small pinhole (20 mils in diameter) and letting the transmitted beamlet travel a long distance ($\sim$1 m) before striking the scintillator where an image is taken. The position of the pinhole defines the coordinates x and y, and from the image we can extract the density distribution of x' and y'. Because of the fact that the beam at the exit of the final-focus system is prepared to focus to small spot in the absence of space charge, a standard pepperpot technique does not work since all the individual beamlets would fall on a single spot. Figure 5 shows schematically this technique along with some images of the individual beamlets that show a very detailed structure of the phase-space distribution. The knowledge of the 4-dimensional phase space is essential in order to run more realistic simulations of the beam focusing to a small spot when drifting through neutralizing plasma.

The primary simulation tool is WARP3D [7]. The code is used to simulate the ion beam from source through the 4-quadrupoles and the neutralized drift section to the target. Details of the experimental setup are incorporated into the code including all electric (electrodes) and magnetic fields (third order nonlinear magnetic fields as calculated by ANSYS). Figure 6 shows the dominant quadrupole and pseudooctupole magnetic fields used in WARP3D for the numerical simulations. In the neutralized drift section, a simple approximation is applied in which the space-charge forces are uniformly reduced by a neutralization factor, of the order of 95% to 97%, which is a result obtained from a more detailed neutralized beam transport calculation using LSP code [6]. LSP models the plasma-beam interaction in detail, while WARP3D is the code of choice for magnetic lattice beam dynamics. The simplifying approximation allows us to extrapolate the beam dynamics effects in the quadrupole section to the final beam spot.

IV. TRANSPORT IN FINAL-FOCUS SYSTEM

A high-brightness, low emittance ion beam is an essential component of the neutralized transport experiment (NTX) to obtain the minimal spot size at the focal plane [Eq. (3)]. An ion beam extracted from a Pierce-type diode suffers from spherical aberrations as evidenced from phase-space distortions (high emittance) and from nonuniform charge density profiles. Since the source of these aberrations are the high order field components, the particles at the edge of the beam are the most affected. One way to generate high-brightness beams is to remove the edge of the beam after it is generated in the diode [6]. To study

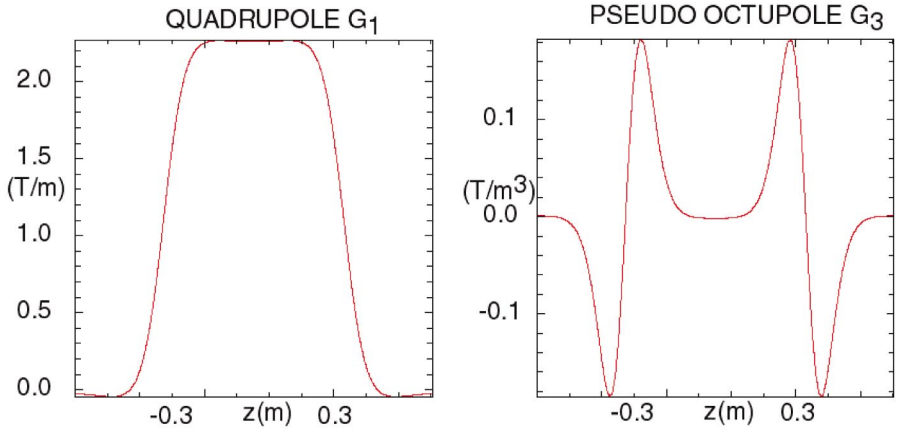

FIG. 6. (Color) Dominant (a) quadrupole and (b) pseudooctupole coefficients for the multipole decomposition $B_\perp(r, \theta, z) = G_1(z) r \cos(2\theta) + G_3(z) r^3 \cos(2\theta) + \ldots$.

beam transport through the final-focus system a 300 keV, 50 mA beam extracted from the diode, has been apertured to a 1 cm, 25 mA beam with a normalized emittance of 0.05 π–mm-mr and a uniform density profile. Figure 7 shows the good agreement between the measured (left) and calculated (right) beam profiles and phase space.

A. Envelope control

A series of measurements were performed to demonstrate the control that WARP3D has in predicting the quadrupole fields to obtain prescribed beam parameters.

The first case was to produce a round beam with the nominal parameters of 20 mm radius and 20 mr convergence (one-meter focal length). Figure 8 shows the good agreement between the measured (top) and calculated (bottom) beam profiles and phase-space distributions at the entrance to the neutralization region. The slight distortion of the beam profile can be traced back to a small rotation (5 mr) of one of the quadrupoles. The beam is uniform with a narrow rim due to field aberrations, and the measured final unnormalized emittance of the beam is $\sim$25 π–mm-mr, small enough to focus the beam to a spot radius of $r_s \sim 1$ mm.

We also compared the beam profiles for several quadrupole strength configurations as calculated by WARP3D and as measured. In Fig. 9, for each quadrupole, the corresponding row shows the profiles for a change of -5%, 0%, and $+5\%$ from the nominal quadrupole strength. This comparison shows the good agreement that we have obtained so far, between measurements and simulations.

In order to study the spot size dependence on convergence angle, we have varied the quadrupoles to obtain various values of the convergence angle θ (5, 10, and 20 mr) for a given beam energy and current. The agreement between theory and experiment is excellent. Finally, the perveance was varied, and the same code-experiment agreement was demonstrated.

As a preliminary test of the NTX system, the beam at the end of the magnetic lattice was injected into a vacuum pipe without any neutralization. Figure 10 shows the measured beam profiles at 1 m downstream from the exit of the final-focus system. The energy varies from 260 to 300 keV, and the beam profiles are in good agreement with WARP3D simulations.

B. Energy scan

We have also performed a complete characterization of the quadrupole lattice by comparing experimental results with particle simulations when the beam energy (and current) was varied. Again, the beam shape varied as predicted by WARP3D, when a 3% energy shift correction is applied. Figure 11 shows the good agreement between the calculated and measured beam size at the exit of the final-focus system when the beam energy is varied. The numerical

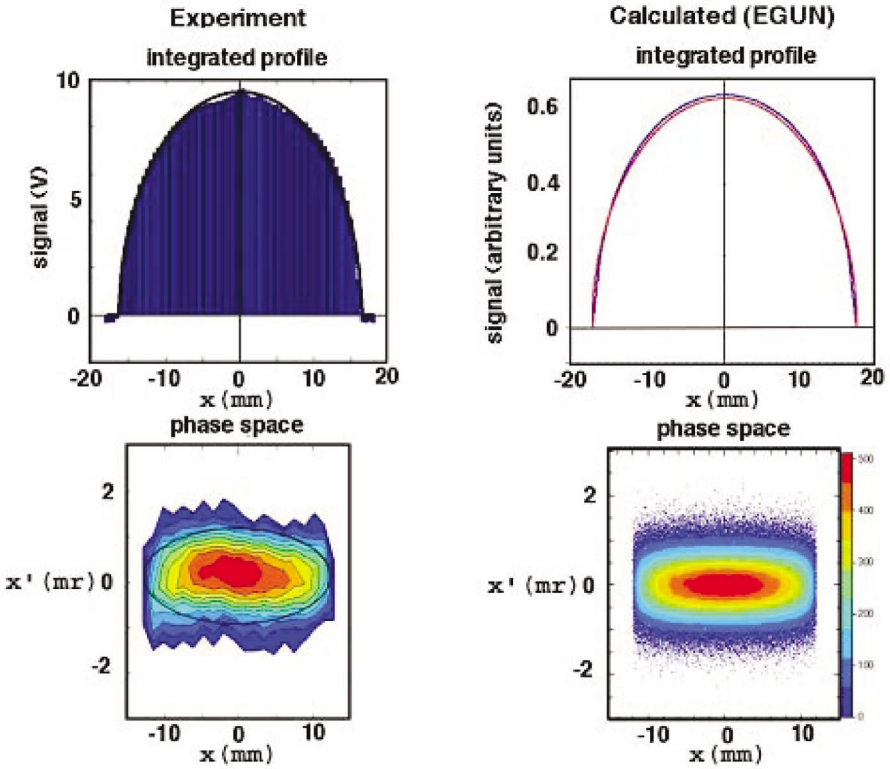

FIG. 7. (Color) Slit-integrated density profile and (x, x') phase space of a high-brightness apertured beam (300 kV, 25 mA, 2-cm aperture diameter). The corresponding EGUN calculations are shown to the right.

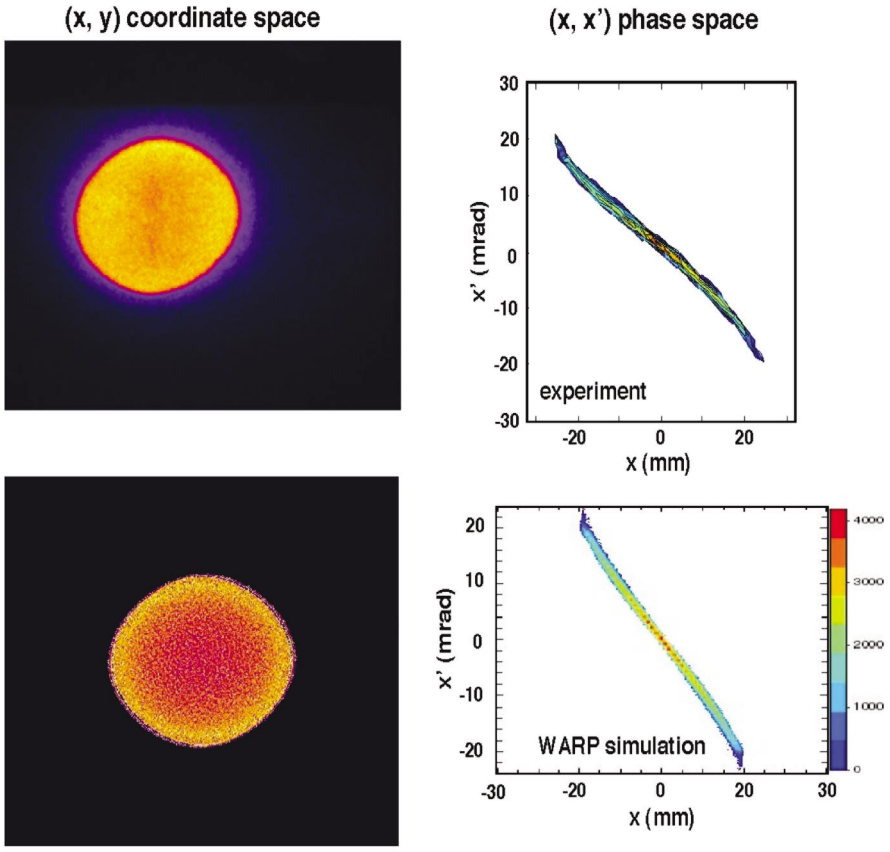

FIG. 8. (Color) Experimental results and simulations of beam profile and phase-space distribution at exit of channel.

simulations track the beam behavior as the beam expands by a large factor when the energy changes from -9% to $+9\%$ around the nominal energy.

The sensitivity of the beam optics to small changes in beam energy was evaluated by measuring the beam size as the energy varied for a given beam slice. We observed that energy variations of 1% led to reduction of current density by 50%. This experimental result is consistent with numerical simulations. Since on NTX there is an uncompensated beam head-to-tail energy and current variation from

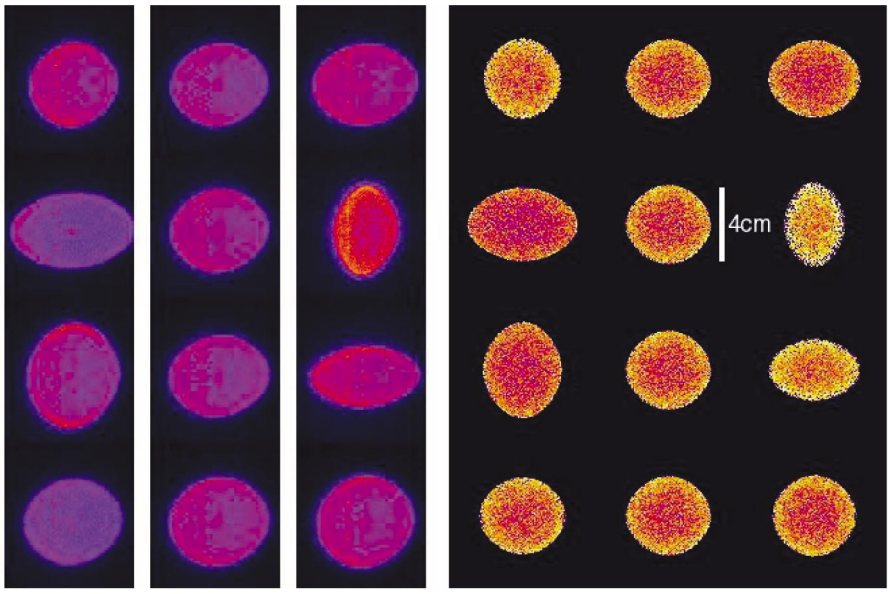

FIG. 9. (Color) Numerical results and camera images of beam profiles as a function of quadrupole field configuration.

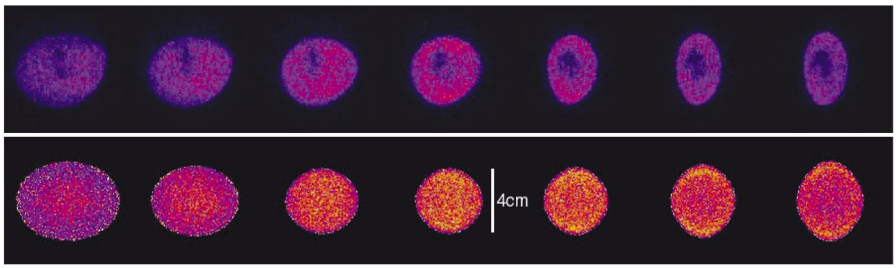

FIG. 10. (Color) Experimental (top) and theoretical (bottom) NTX beam profiles for a nonneutralized beam 1 m downstream from the exit of the final-focus system.

initial transients in the injector, we also measured directly the spot size variation from head to tail (Fig. 12), where significant changes were observed. The voltage (energy) waveform shows a variation of ~1%, and this energy variation is enough to account for the head-to-tail variation in spot size. For future work, we need to study the energy sensitivity for other lattices (e.g., 6-quad lattice) to see if the energy sensitivity could be reduced. Also, time-dependent focusing may be used to correct for the head-to-tail variations.

C. Geometric aberrations

The goal of a final-focus experiment is to obtain the minimal spot radius. Equation (2) suggests that one could reduce the spot size by increasing the convergence angle, provided that the emittance is not significantly increased. In general, as the angle is increased, the beam envelope goes through larger excursions in the magnetic lattice, which in turn leads to increase in emittance through higher order (particularly third order) aberrations. The distortion of phase space due to geometric aberrations has been studied numerically. In this experiment, we see the same phase-space distortions, leading to increased spot size with large angles. Both code and experiment predict minimum spot radius at ~15 mrad (Fig. 13). Equation (6) predicts a monotonically increasing spot size as the convergence angle is varied, but in the experiments, however, the results are complicated by nonoptimal entrance conditions from the apertured source which is the same for the different magnet tunes. In fact for the NTX lattice and for fixed entrance conditions, the emittance growth along the lattice may be larger for smaller convergence angles.

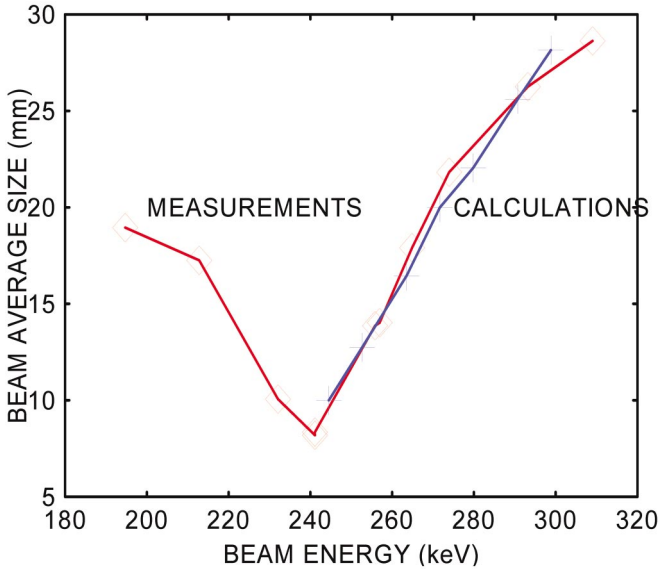

FIG. 11. (Color) Calculated (blue plus sign) and measured (red diamond) beam size at the exit of the final-focus system as the beam energy is varied. A factor of 3% was subtracted from the energy used in the calculation.

D. Spot size dependence on perveance

Finally, we consider variations of perveance. In general, we expect the geometric aberrations to be less significant for lower perveance beams. This is true if the final-focus lattice is ''matched'' to the beam perveance; it is always possible to design a final-focus system for a lower perveance beam that will be less affected by geometric aberrations. The NTX lattice was designed for the 25 mA potassium beam at 300 keV, with perveance $Q \sim 0.0006$.

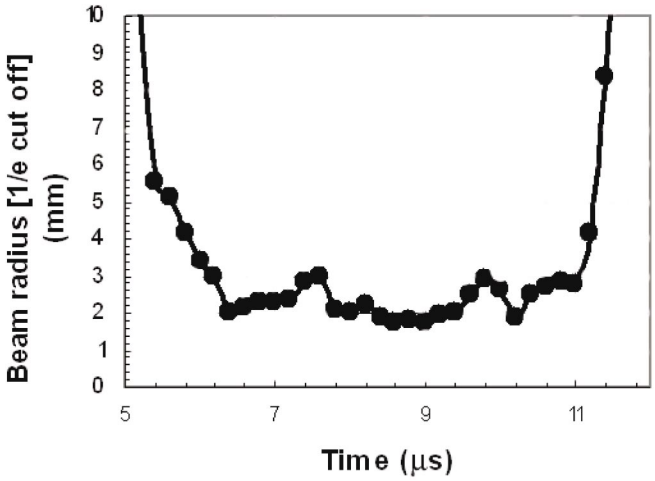

FIG. 12. Spot size variation from head to tail measured at the focal plane, showing blow up of the beam head and tail.

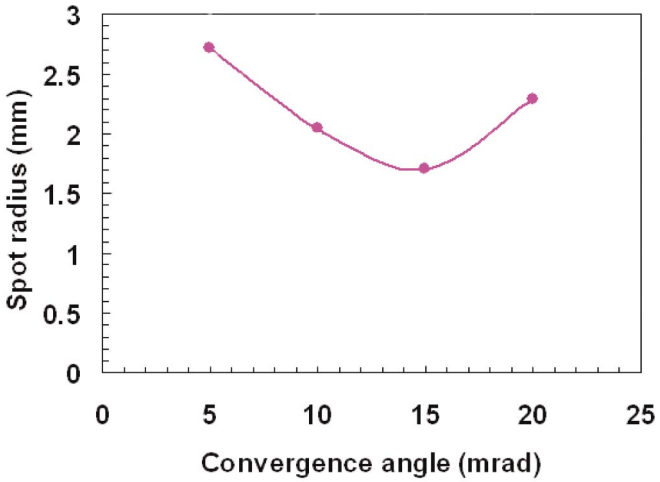

FIG. 13. (Color) Spot size as function of convergence angle.

Figure 14 shows the spot size dependence on perveance by comparing the beam images at the focal plane for a 264 keV beam that has been apertured to 25 and 6 mA, respectively, and that are transported through the final-focus system using the same quadrupole fields. There is a large reduction in spot size for the lower perveance beam.

It is important to point out that the low emittance ($\sim$25 π–mm-mr unnormalized) of the beam at the entrance to the neutralized region allows for the beam to be focused to a small spot size (1–2 mm radius) at the focal plane for neutralized ballistic transport. Furthermore, Faraday cup measurements of the beam current at entrance and exit of the final-focus system have shown negligible beam loss along the transport channel.

The pinhole diagnostics system described in Sec. 3 can be used to simulate the effect of full neutralization on a beam, since each beamlet going through a pinhole only carries the information about the phase-space distribution at a given location without being perturbed by the space charge of the full beam. The superposition of all the pinhole images at a given location can be compared with a beam transport calculation where the space charge is turned off from the pinhole-scan plane to the focal plane. Figure 15 shows a comparison between this "analog experiment" and WARP3D simulations; the agreement is excellent and shows that the emittance is low enough to get a small spot (~1 mm radius).

While we have very good agreement between theory and experiment in many aspects, there are several observations, which are not yet well understood. We have mentioned the need for an arbitrary energy calibration factor in order to obtain agreement between theory and code. To refine the energy calibration in the experiment, we performed a series of time-of-flight (TOF) experiments, as well as careful calibration of resistive and capacitive monitors. While the 3 different ways of energy calibration agree within the experimental uncertainties, the discrepancy with theory persists.

In pursuit of the explanation of this discrepancy, we suspect that stray electrons might play a role. To ascertain this effect, we incorporated a mesh liner along the pipe. However, while currents were clearly collected on the mesh, its net effect on the beam profile was relatively minor.

Finally, we have observed clear evidence of halo formation, in both configuration space (Fig. 16) and velocity space (Fig. 17) as evidenced by the rings surrounding the central image. However, we have not been able to account, from numerical simulations, for the origin of these halo particles thus far.

V. ERROR ANALYSIS

In this section, we discuss several factors that may influence our interpretation of the ion beam data. To quantify these effects, a series of experiments were performed. These include: (a) stray electron effects on the beam inside the quadrupole lattice, (b) calibration of beam energy, (c) measurements of quadrupoles field strength, and (d) efficiency of the diagnostic devices.

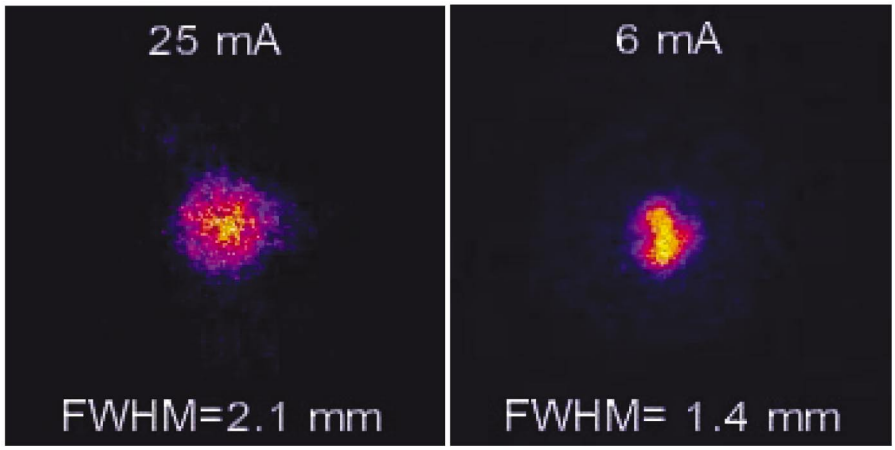

FIG. 14. (Color) Spot size dependence on perveance.

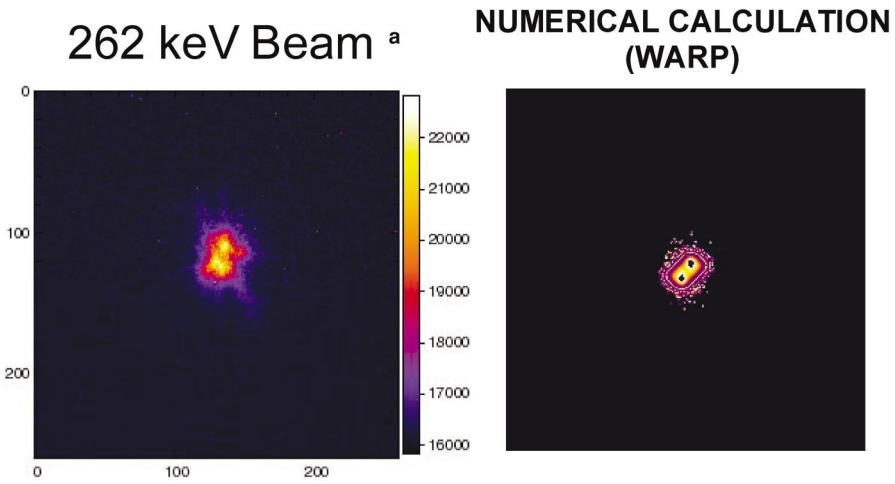

FIG. 15. (Color) Analog (pinhole) simulation and WARP3D calculation of fully neutralized beam focused to a small spot. Image box size is 4 cm $b \times 4$ cm squares.

A. Stray electron effects inside the quadrupole lattice section

As we mentioned in Sec. 3 the NTX magnetic transport section contains an aperturing system for variable perveance, brightness, and beam size. This aperturing technique is provided with a sandwich-type electron trap to collect electrons. Ions from the poorly matched beam head and halo ions in the main pulse of the beam can strike the outer wall of the beam tube. A single ion impact can produce thousands of secondary electrons depending on the energy and angle of incidence, with ions of grazing-angle incidence producing the largest secondary electron yields. Only a small fraction of the beam ions striking the wall are needed to provide a space-charge-limited supply of electrons from the wall. If the secondary electrons are not stopped, they are attracted by the beam potential and can provide some degree of beam neutralization. The presence of wall electrons was measured using a long radial metal mesh, which was installed inside the magnetic drift section. Mesh radial diameter, space of wire and mesh length were 23.5 cm, 1.27 cm, and 2.28 m, respectively.

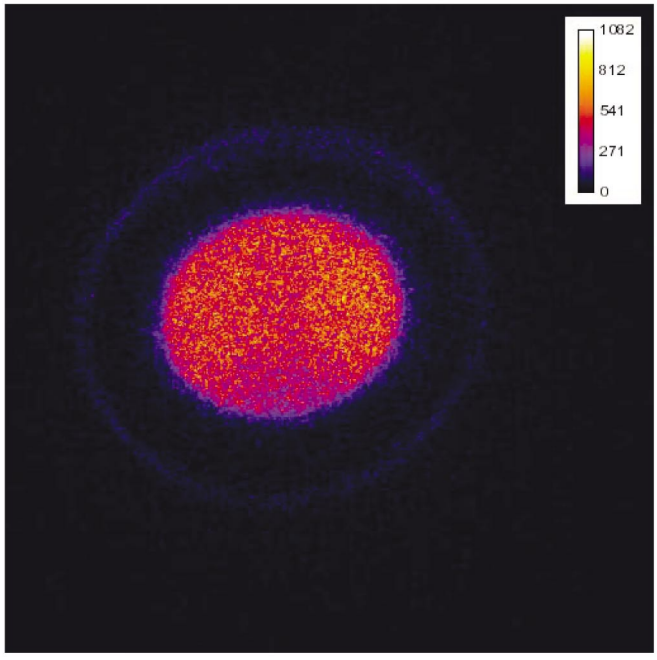

FIG. 16. (Color) Evidence of beam halo formation in configuration space. Image for a 6% off-energy beam, measured at end of the final-focus system (beam size ~2 cm).

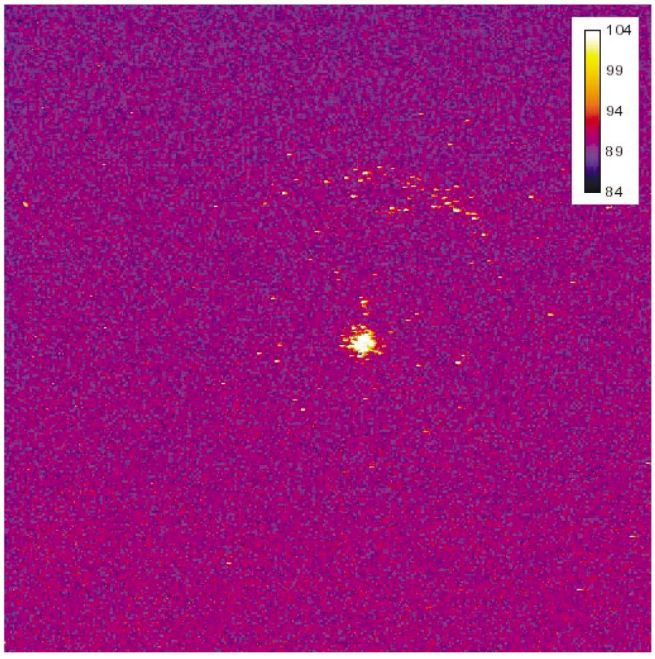

FIG. 17. (Color) Evidence of beam halo formation in velocity space. Image from a pinhole positioned at end of the final-focus system and at the center of the beam, and measured at the focal plane.

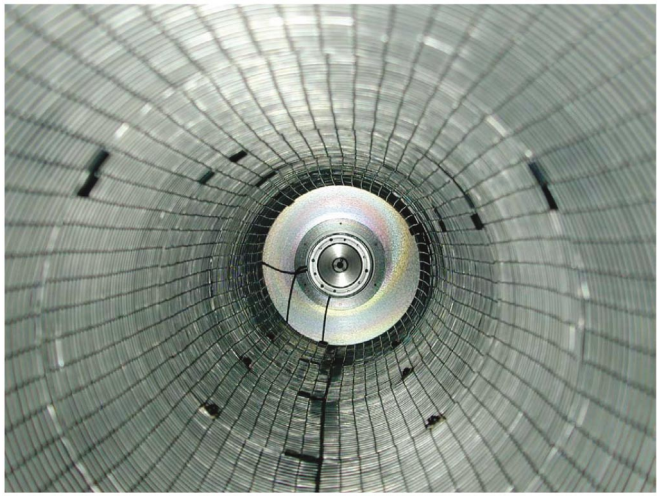

FIG. 18. (Color) A cylindrical metal mesh inside the beam pipe in the magnetic final-focus section.

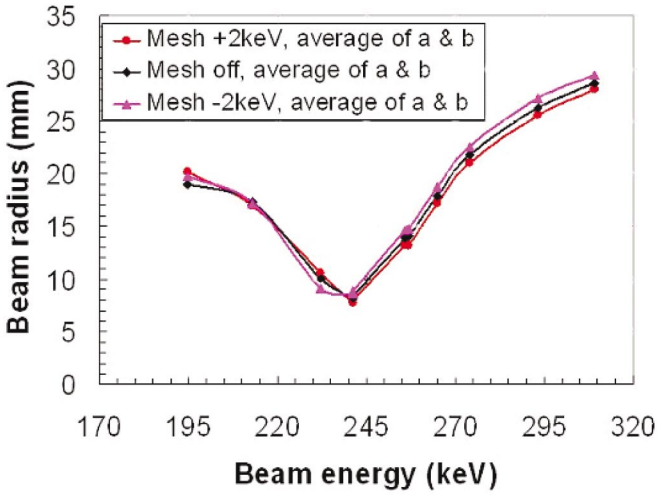

FIG. 20. (Color) Beam radius as a function of beam energy as mesh bias is turned on ($\pm$ 2 kV) and off.

Figure 18 shows the 23.5 cm diameter metal mesh inside the magnetic transport section, which was biased with a ± 2 kV potential. Beam profile at the scintillator, located at the end of the final-focus magnets, and current in the mesh as a function of the mesh voltage were measured. Figure 19 shows the measured current in the mesh by varying its bias voltage.

As a negative voltage was applied across the mesh, there was no significant current measured in the mesh. It shows that there was no significant number of ions from the beam halo near the beam pipe wall. When the voltage was switched to positive, significant current in the mesh was measured. It shows that wall electrons were collected in the positive biased mesh. These electrons were generated in the drift tube wall. But the beam was not significantly affected by electrons. Figure 20 shows beam radii corresponding to several beam energies in condition of mesh bias powered to ± 2 kV and without any mesh voltage. By comparing these 3 cases, we see that the beam radius changes were not significant. It is inferred that for a large pipe, the wall electrons spend only a small fraction of their time within the beam. The electrons were moving at their greatest velocity while passing through the beam, reducing their net effect of beam neutralization.

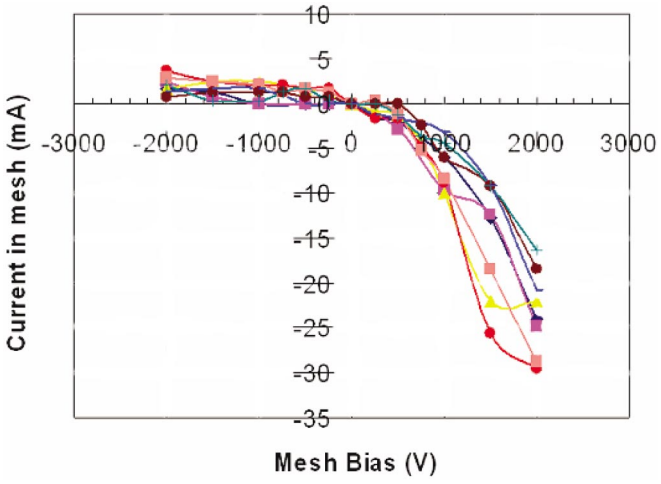

FIG. 19. (Color) Mesh current when applying voltage across the mesh. Different lines correspond to different energies, ranging from 244 to 320 keV.

Though a mesh inside the final-focus magnetic section was not necessarily effective due to the large diameter of the beam pipe, it provided good evidence that a positively biased metal mesh can reduce beam neutralization due to stray electrons. This effect can be very significant in a small size drift tube, as we have found in the neutralized drift section with its 3 in. diameter pipe [6].

B. Calibration of energy

The NTX source is powered from a Marx generator as mentioned in the experimental Sec. 3. This voltage is measured with a capacitive voltage divider. Calibration of beam energy is important because of the sensitivity of beam transport to the beam energy in a quadrupole transport channel as we have shown in Sec. IV. To provide a cross check of the beam energy measurement, the capacitive system, was compared to time-of-flight measurements and a resistive voltage divider system.

Charged particle beams are capable of supporting and transmitting a variety of waves. Longitudinal space-charge waves are longitudinal oscillations of the beam within the conducting boundary of a vacuum wall. These waves have been studied and applied to continuous electron beams in microwave devices, bunched charged particle beams in particle accelerators, and space-charge dominated charged particle beams. The theoretical equilibrium and stability of these waves have been explored extensively. Here we discuss a diagnostic technique that utilizes longitudinal space-

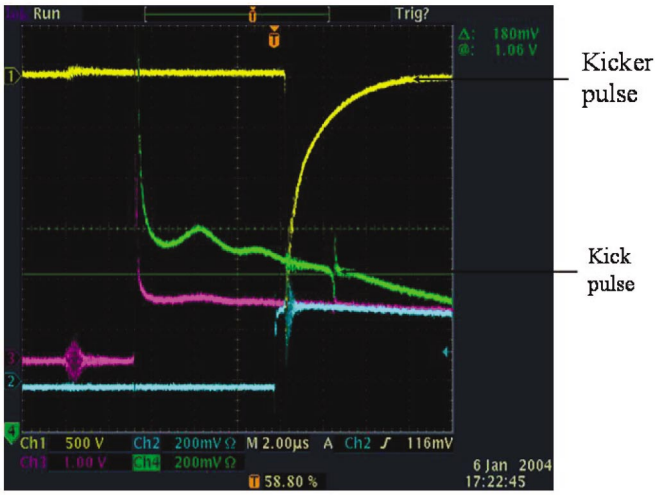

FIG. 21. (Color) Typical waveforms of kicker (yellow trace) and kick (green trace) pulses for time-of-flight measurements. The oscilloscope vertical scale is arbitrary, the horizontal scale is 2 μs per division. The magenta and blue traces are auxiliary traces captured in this image.

charge waves in heavy-ion beams to determine beam energy by TOF.

The TOF method described here is to longitudinally perturb a slice of the beam with a fast voltage pulse applied to a ''kicker'' near the path of the beam. The kicker may be any cylindrically symmetric mechanical structure near the beam that can rapidly generate a localized longitudinal electric field on the beam. A typical kicker and kick pulses are shown in Fig. 21. The voltage pulse applied to the kicker locally perturbs the energy of the beam particles passing near the structure. The perturbation propagates in the form of a wave that travels with the beam. In the long wavelength limit, there is a fast wave traveling toward the front of the beam pulse and a slow wave traveling toward the rear. Measuring the arrival time of the resulting space-charge wave at a detector placed a suitable distance downstream provides a measure of the beam energy.

The structure utilized as a kicker is a thin aperture which also limits the beam transversely for the final-focus experiments. The NTX TOF pulse has a rise time of about 4 ns, a fall time of about 1 μs, and the peak output voltage is -2.5 kV. The path length between the kicker and registering beam current at a Faraday cup is 2.48 m.

The initial pulse resembles the longitudinal electric field (spatial derivative of the potential perturbation) at the kicker. Beam ions are spread apart at the front of the wave and compressed at the rear. The result is a double pulse which is very well defined in time. The time reference for TOF measurements is the point in which the wave passes through zero. This corresponds to those particles which were at the location of the aperture at the time that the pulser voltage is turned on.

The comparison between data and the 1D model is shown in Fig. 22 for a small current (1 mA). The agreement between model and data is good. However, for a large current (25 mA) the discrepancy varies. Figure 23 shows the relative difference between TOF beam energy (open squares), resistive divider voltage (diamonds), and capacitive divider voltage readings as a function of NTX Marx voltage. Both TOF and resistive divider measurements are shown as a function of capacitive divider voltage. 2% error bars are assumed for both sets of measurements. A linear fit to the data points is also shown for each set of measurements. The voltage indicated by the resistive divider lies between the capacitive divider and the TOF measurements.

C. Field of the 4 quadrupole magnets

The strength of the 4 quadrupole magnets is provided by 4 separate power supplies using a pulser. Waveforms of each power supply are monitored on an oscilloscope screen. There is a $\pm 0.5\%$ magnetic field error bar when measured on wave forms displayed on the oscilloscope.

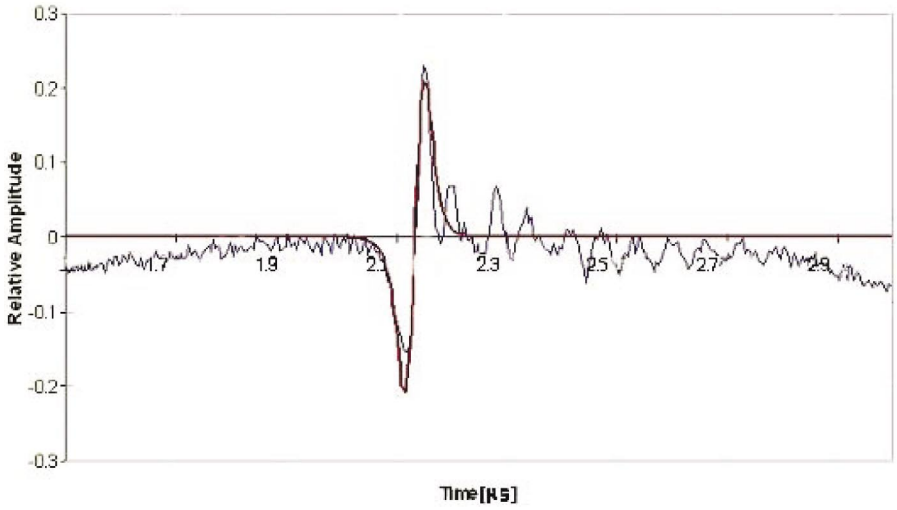

FIG. 22. (Color) Space-charge wave in NTX for a low-current beam.

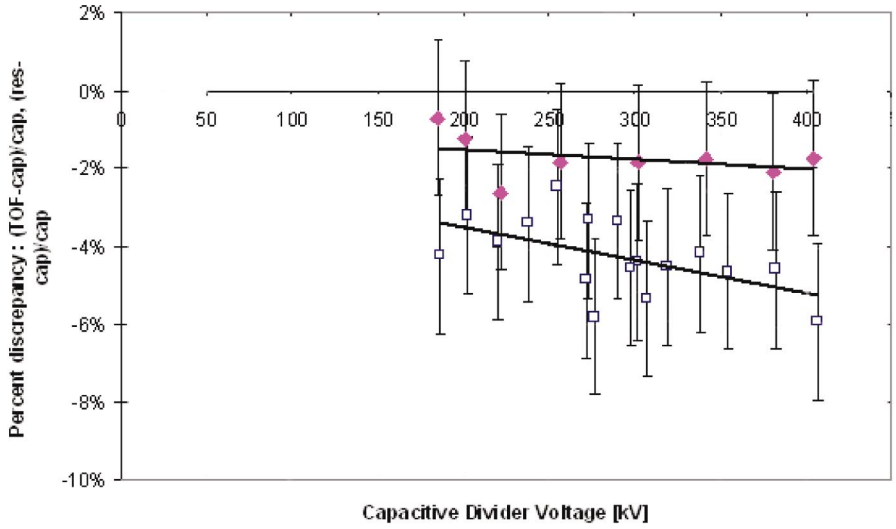

FIG. 23. (Color) The relative difference between TOF beam energy (open squares), resistive divider voltage (diamonds), and capacitive divider voltage readings (0% line) as a function of NTX Marx voltage. Both TOF and resistive divider measurements are shown as a function of capacitive divider voltage. 2% error bars are assumed for both sets of measurements. A linear fit to the data points is also shown for each set of measurements. The voltage indicated by the resistive divider lies between the capacitive divider and the TOF measurements.

Moreover, the magnet current monitor is a current transformer with an accuracy specification of $+1\%$ and -0%. The existing timing setup assumes that the peak quadrupole field occurs at the peak of the monitored magnet current. In reality, there is attenuation and a time shift because of the diffusion of the magnetic field through the 3.3 mm pipe wall. This phase shift is approximately 275 μs based on ANSYS 2D transient EM finite element modeling. Because of this time shift, the timing of the beam may not be during the peak quadrupole field. By the same modeling, the peak field is attenuated by approximately 7% and has been considered in setting the magnet currents.

D. Efficiency of diagnostic devices

As was mentioned in Sec. 3, the diagnostics that have been used in this experiment are Faraday cups, slit cups, and scintillators associated with electronics and a CCD gated camera. Though slit cups have available an electron guard ring, there exists the possibility of the generation of secondary electrons noise by energetic particles, whose presence can mislead the interpretation of halo particles studies. Moreover, once energetic particles strike on a scintillator, its efficiency degrades as a function of incoming beam particle energy.

VI. CONCLUSIONS

The key question of a final-focus experiment is what determines the spot size. In this paper, the emphasis is on the role of the final magnetic system. The effects of plasma neutralization dynamics are discussed elsewhere.

We have shown from both theory and experiment on how to prepare the beam envelope for final neutralized drift. We have also studied the effects of beam energy variations and demonstrated the importance of head-to-tail energy uniformity. We have studied the higher order aberrations, and, in particular, the geometric aberrations and its effect on the spot size. Finally, we have considered the dependence of spot size on perveance.

Overall, the comparisons between theory and experiment are quite good. We have discussed some possible factors in the experiment which are not included in the theory, and an attempt to resolve these issues experimentally.

In terms of future experimental work, the most important task is an *in situ* measurement of the magnetic field, including all the eddy current effects of the pipe and flanges.

One additional unexplained observation has to do with haloes in both configuration and velocity space. We presented two examples in Figs. 16 and 17, respectively. Numerical simulations have not been able to account for these haloes thus far, and will be the subject of future studies.

While we still have a couple of puzzles to resolve, we believe that much has been learned about the final-focus magnetic system relevant for a HIF driver. The questions of how to control energy sweep, design constraints on aberrations, and perveance, are now much better understood as a result of this work.

ACKNOWLEDGMENTS

This work was performed under the auspices of the U.S. Department of Energy by University of California Lawrence Berkeley National Laboratory under Contract No. DE-AC03-76SF00098; E. Henestroza was also sup-

ported by Department of Energy, Office of Fusion Energy Science, Grant No. DE-FG02-01-ER54662.

[1] D. Neuffer, in *Proceedings of the Heavy Ion Fusion Workshop, Argonne National Laboratory, 1978* (Argonne National Laboratory Report No. ANL-79-41, 1978), p. 333.

[2] E. Colton, in *Proceedings of the Heavy Ion Fusion Workshop, Argonne National Laboratory, 1978* (Argonne National Laboratory Report No. ANL-79-41, 1979), pp. 365–378.

[3] A. A. Garren, in *Proceedings of the ERDA Summer Study for Heavy Ions for Inertial Fusion, 1976*, edited by R. O. Bangerter, W. B. Herrmannsfeldt, D. L. Judd, and L. Smith (Lawrence Berkeley National Laboratory Report No. LBL-5543, 1976), pp. 102–109.

[4] D. D.-M. Ho, I. Haber, K. R. Crandall, and T. S. Brandon, Particle Accelerators **36**, 141 (1991).

[5] S. MacLaren, A. Faltens, and P. A. Seidel, Phys. Plasmas **9**, 1712 (2002).

[6] E. Henestroza *et al.*, Phys. Rev. ST Accel. Beams **7**, 083501 (2004).

[7] D. P. Grote, A. Friedman, G. D. Craig, W. M. Sharp, and I. Haber, Nucl. Instrum. Methods Phys. Res., Sect. A **464**, 563 (2001).

[8] I. M. Kapchinskij and V. V. Vladimirskij, in Proceedings of the 1959 International Conference on High Energy Accelerators. Geneva, Switzerland: CERN, 1959.

[9] E. P. Lee, Lawrence Berkeley National Laboratory Report No. LBL-28463, 1991.

[10] D. Baca, J. W. Kwan, and J. K. Wu, in *Proceedings of the 2003 Particle Accelerator Conference*, edited by J. Chew, P. Lucas, and S. Webber (IEEE, Piscataway, NJ, 2003), p. 3294.

[11] W. M. Fawley, T. Garvey, S. Eylon, E. Henestroza, A. Faltens, T. J. Fessenden, K. Hahn, L. Smith, and D. P. Grote, Phys. Plasmas **4**, 880 (1997).

[12] D. Shuman, S. Eylon, E. Henestroza, P. K. Roy, W. Waldron, S. S. Yu, and T. Houck, in *Proceedings of the 2003 Particle Accelerator Conference*, edited by J. Chew, P. Lucas, and S. Webber (IEEE, Piscataway, NJ, 2003), p. 2628.